Fully unconstrained noncollinear magnetism within the PAW method

D. Hobbs, G. Kresse and J. Hafner

Institut für Materialphysik and Centre for Computational Material Science, Sensengasse 8/12,
A-1090 Wien, Austria

Introduction

In recent years a great deal of effort has been focused on developing the so called "fully unconstrained" approach to noncollinear magnetism. This approach allows the magnetisation density within a material to be calculated as a continuous vector variable of position as opposed to using the atomic moment approximation (AMA) where a fixed quantisation direction is assumed for a volume filling sphere surrounding each atomic site i.e. the constrained approach. The motivation for a fully unconstrained approach is to allow the magnetisation density to be correctly treated in the interstitial regions between atomic sites. While many materials have well localised magnetisation densities for which the AMA is valid, others (including the spin spiral ground-states of rare earths, topologically frustrated systems such as triangular monolayers and Kagomé lattices, spin-glasses, materials containing domain walls and/or at finite temperatures) may exhibit a de-localised magnetisation density which is more appropriately treated with a fully unconstrained approach.

Oda *et al.* [1] were the first to implement such an approach within a plane-wave pseudopotential scheme. Both the atomic and magnetic structure were allowed to relax simultaneously and self-consistently. Their method was applied only to small Fe clusters, which have less symmetry constraints than the bulk thus making them good candidates for noncollinear magnetic arrangements. Ivanov and Antropov [2] developed a wavelet technique for calculating the electronic and noncollinear magnetic structures in the framework of spin-density functional theory again without imposing shape restrictions to the magnetisation density. Their preliminary report studied the spin-structures of H_3 and Cr_3 clusters.

In parallel with our efforts here in Vienna, Nordström and Singh [3], Asada *et al.* [4] and Kurz *et al.* [5] have concentrated on developing the method within the full-potential linearised

augmented plane-wave (FLAPW) formalism. The approach of Nordström and Singh [3] is fully unconstrained in the sense discussed above while that of Asada *et al.* [4] and Kurz *et al.* [5] is adapted to suit the film geometry for surfaces and open structures. This adaptation imposes a constraint. The magnetisation density is treated as a continuous vector field in the interstitial region and in vacuum, while inside each muffin-tin sphere they allow only a fixed spin-quantitation axes. Since in the FLAPW the muffin-tin spheres are significantly smaller than the volume filling atomic spheres this extra constraint is probably a reasonable one.

Our objective has been to implement a fully unconstrained approach within the projector augmented wave (PAW) method. The PAW approach [6, 7] is an all-electron method for electronic-structure, total-energy and force calculations which is closely related to the ultrasoft-pseudo-potential technique [8, 9]. In the PAW approach, charge- and spin-densities are decomposed into pseudo- and compensation densities accounting for the difference between the pseudo- and all-electron densities (see Fig. 1). The pseudo-densities consist of a smooth part expressed in a plane-wave representation and localised compensation charges accounting for the violation of norm-conservation [8, 9]. To account for differences between pseudo- and all-electron densities radial support grids are used. For each of the atom-centred radial support-grids the spin-quantisation axis is fixed - in this respect our approach resembles the unconstrained noncollinear FLAPW technique used by Asada *et al.* [4] and Kurz *et al.* [5], but unlike to the FLAPW method, in the PAW approach the plane-wave description is not restricted to the interstitial region, but extends over the complete volume of the system. Hence variations of the magnetisation direction are allowed also within the augmentation spheres. Our method allows both the atomic and magnetic structures to relax simultaneously and selfconsistently. The algorithms have been implemented within the Vienna ab-initio simulation package (VASP [10]). Below we present only a brief summary of the noncollinear PAW formalism, for a detailed discussion we refer the reader to Hobbs *et al.* [11]. Our results for small metallic clusters derive from Ref. [11] while the results for Cr and Mn on Cu(111) substrates are detailed in Ref. [12].

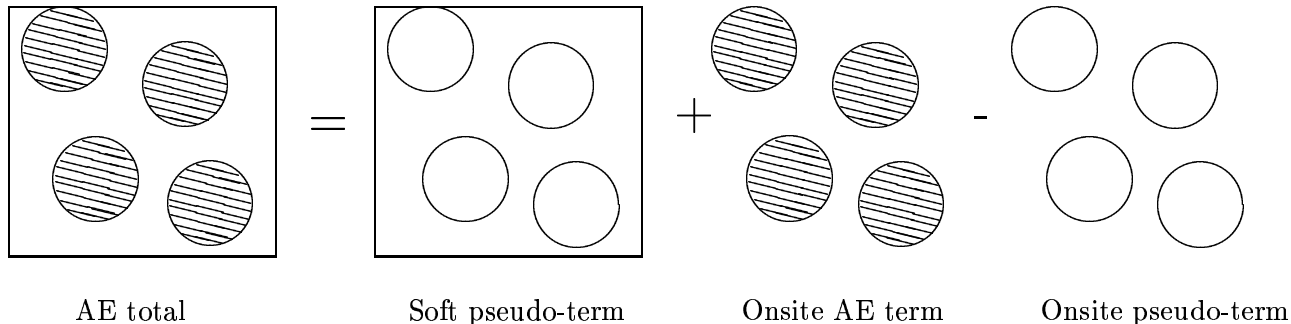AE total   Soft pseudo-term   Onsite AE term   Onsite pseudo-term

Figure 1: Illustration of the PAW approach. The AE charge density is constructed by modifying the total soft pseudo charge density by replacing the onsite pseudo-charge density with the onsite AE charge density. The same concept holds for wavefunctions, total energy and the Hamiltonian.

LSDF theory for noncollinear PAW

A generalisation of von Barth and Hedin's [13] local-spin-density-functional (LSDF) theory to noncollinear magnetism was first proposed by Kübler *et al.* [14, 15] within the framework of the

augmented-spherical-wave (ASW) method and the atomic-sphere-approximation. The effective single-particle equations for noncollinear magnets were derived by allowing the spin-quantisation axis to vary from site to site in crystalline systems. The orientation of the axis with respect to the reference frame is a property of the ground-state. They predicted well defined sets of directions for the spins, which are uncoupled from the crystal lattice unless spin-orbit coupling effects are included in the Hamiltonian (even though such effects are small in comparison to the spin-spin interactions).

Following Kübler *et al.* [14, 15], spin-polarised density functional theory is expressed in terms of a 2×2 density matrix with elements $n^{\alpha\beta}(\mathbf{r})$, where α and β refer to the spin indices. The electron density is then

$$\mathrm{Tr}\left[n^{\alpha\beta}(\mathbf{r})\right] \equiv n_{\mathrm{Tr}}(\mathbf{r}) = \sum_{\alpha} n^{\alpha\alpha}(\mathbf{r}). \tag{1}$$

The total density matrix may then be defined as

$$n^{\alpha\beta}(\mathbf{r}) = \left(n_{\mathrm{Tr}}(\mathbf{r})\delta_{\alpha\beta} + \vec{m}(\mathbf{r}) \cdot \vec{\sigma}^{\alpha\beta}\right)/2. \tag{2}$$

In addition, for the density matrix, we can make a transformation to the equivalent magnetisation density using the following formula [16]:

$$\vec{m}(\mathbf{r}) = \sum_{\alpha\beta} n^{\alpha\beta}(\mathbf{r}) \cdot \vec{\sigma}^{\alpha\beta}, \tag{3}$$

where $\vec{\sigma} = (\sigma_x, \sigma_y, \sigma_z)$ are the Pauli spin matrices. The exact Kohn-Sham density functional becomes (we use atomic units, $\hbar = m = e^2 = 1$)

$$E = \sum_{\alpha}\sum_{n} f_n \langle \Psi_n^\alpha | -\frac{1}{2}\Delta|\Psi_n^\alpha\rangle + E_H[n_{\mathrm{Tr}} + n_Z] + E_{xc}[n^{\alpha\beta}]. \tag{4}$$

$E_H[n_{\mathrm{Tr}}+n_Z]$ is the electrostatic energy of the electronic charge density n_{Tr} and the point charge densities of the nuclei n_Z and is defined by

$$E_H[\wp] = \frac{1}{2} \int \int \frac{\wp(\mathbf{r})\wp(\mathbf{r}')}{|\mathbf{r} - \mathbf{r}'|} d\mathbf{r} d\mathbf{r}', \tag{5}$$

where $\wp = n_{\mathrm{Tr}} + n_Z$. $E_{xc}[n^{\alpha\beta}]$ is the electronic exchange-correlation energy and f_n are orbital occupation numbers. The exchange-correlation energy is not known in general, but only for a spin-polarised homogeneous electron gas with charge density n_{Tr} and magnetisation density $\vec{m}$. In the local-spin-density approximation $E_{xc}[n^{\alpha\beta}]$ is defined by:

$$E_{xc}[n^{\alpha\beta}] = \int n_{\mathrm{Tr}}(\mathbf{r})\epsilon_{xc}[n^{\alpha\beta}(\mathbf{r})]d\mathbf{r} = \int n_{\mathrm{Tr}}(\mathbf{r})\epsilon_{xc}[n_{\mathrm{Tr}}(\mathbf{r}), |\vec{m}(\mathbf{r})|]d\mathbf{r}. \tag{6}$$

The exchange-correlation functional leads to the nonmagnetic scalar exchange-correlation potential, v_{xc}, and to the magnetic exchange-correlation field $\vec{b}\left[n^{\alpha\beta}\right](\mathbf{r})$. The potential $\vec{b}\left[n^{\alpha\beta}\right](\mathbf{r})$ is parallel to the magnetisation density $\vec{m}(\mathbf{r})$ everywhere. The actual functional form of ϵ_{xc} can be parameterised in several ways (see Hobbs *et al.* [11]).

In the PAW method, the AE wavefunction Ψ_n^α is derived from the pseudo-wavefunction $\tilde{\Psi}_n^\alpha$ by means of a linear transformation [6]:

$$|\Psi_n^\alpha\rangle = |\tilde{\Psi}_n^\alpha\rangle + \sum_i(|\phi_i\rangle - |\tilde{\phi}_i\rangle)\langle\tilde{p}_i|\tilde{\Psi}_n^\alpha\rangle. \tag{7}$$

The pseudo-wavefunctions $\tilde{\Psi}_n^\alpha$ are the variational quantities. The index i is a shorthand for the atomic site $\mathbf{R}$, the angular momentum quantum numbers $L = l, m$ and an additional index k referring to the reference energy ϵ_{kl}. For noncollinear magnetism we define the pseudo-wavefunctions to consist of 2N eigenspinors, where N is the total number of eigenvalues. In our implementation, the pseudo-wavefunctions are expanded in reciprocal space into plane waves

$$\langle \mathbf{r} | \tilde{\Psi}_n^\alpha \rangle = \frac{1}{\Omega_r^{\frac{1}{2}}} \sum_{\mathbf{k}} C_{n\mathbf{k}}^\alpha (\mathbf{r}) e^{i\mathbf{k} \cdot \mathbf{r}}, \tag{8}$$

where Ω_r is the volume of the Wigner-Seitz cell. The AE partial waves ϕ_i are obtained for a nonmagnetic reference atom, the pseudo-partial waves $\tilde{\phi}_i$ are equivalent to the AE partial waves outside a core radius r_c^l and match continuously onto ϕ_i inside the core radius. The core radius r_c^l is usually chosen approximately around half the nearest neighbour distance. The projector functions $\tilde{p}_i$ are dual to the partial waves:

$$\langle \tilde{p}_i | \tilde{\phi}_j \rangle = \delta_{ij}. \tag{9}$$

Starting from Eq. (7) it is possible to show that in the PAW method, the AE total density matrix is given by (for details we refer to Ref. [6]):

$$n^{\alpha\beta}(\mathbf{r}) = \tilde{n}^{\alpha\beta}(\mathbf{r}) + {}^1n^{\alpha\beta}(\mathbf{r}) - {}^1\tilde{n}^{\alpha\beta}(\mathbf{r}), \tag{10}$$

where $\tilde{n}$ is the soft pseudo-density matrix calculated directly from the pseudo-wavefunctions on a plane-wave grid (see Eq. (9) above and Eq. (15) of Ref. [6]) :

$$\tilde{n}^{\alpha\beta}(\mathbf{r}) = \sum_n f_n \langle \tilde{\Psi}_n^\beta | \mathbf{r} \rangle \langle \mathbf{r} | \tilde{\Psi}_n^\alpha \rangle. \tag{11}$$

The on-site density matrices ${}^1n$ and ${}^1\tilde{n}$ are treated on a radial support grid that extends up to r_{rad} around each ion. They are defined as (Eq. (16) and (17) of Ref. [6]):

$$^1n^{\alpha\beta}(\mathbf{r}) = \sum_{(i,j)} \rho_{ij}^{\alpha\beta} \langle \phi_i | \mathbf{r} \rangle \langle \mathbf{r} | \phi_j \rangle, \tag{12}$$

$$^1\tilde{n}^{\alpha\beta}(\mathbf{r}) = \sum_{(i,j)} \rho_{ij}^{\alpha\beta} \langle \tilde{\phi}_i | \mathbf{r} \rangle \langle \mathbf{r} | \tilde{\phi}_j \rangle. \tag{13}$$

$\rho_{ij}^{\alpha\beta}$ are the occupancies of each augmentation-channel (i, j) and they are calculated from the pseudo-wavefunctions applying the projector functions:

$$\rho_{ij}^{\alpha\beta} = \sum_n f_n \langle \tilde{\Psi}_n^\beta | \tilde{p}_i \rangle \langle \tilde{p}_j | \tilde{\Psi}_n^\alpha \rangle. \tag{14}$$

For a complete set of projectors the charge density ${}^1\tilde{n}$ is exactly the same as $\tilde{n}$ within the augmentation spheres. In the PAW approach, the pseudo-wavefunctions $\tilde{\Psi}_n^\alpha$ fulfil the following generalised orthogonality condition:

$$\sum_\alpha \langle \tilde{\Psi}_n^\alpha | S^{\alpha\alpha} | \tilde{\Psi}_m^\alpha \rangle = \delta_{nm}, \tag{15}$$

where the overlap operator is defined by:

$$S^{\alpha\beta}[\{\mathbf{R}\}] = \delta_{\alpha\beta} \left(1 + \sum_i |\tilde{p}_i\rangle q_{ij} \langle \tilde{p}_j| \right), \tag{16}$$

and q_{ij} is given by:

$$q_{ij} = \langle \phi_i | \phi_j \rangle - \langle \tilde{\phi}_i | \tilde{\phi}_j \rangle \qquad (17)$$

The pseudo-wavefunctions are obtained by solving the generalised Kohn-Sham equations

$$\sum_\beta H^{\alpha\beta} | \tilde{\Psi}_n^\beta \rangle = \epsilon_n S^{\alpha\alpha} | \tilde{\Psi}_n^\alpha \rangle. \qquad (18)$$

Forces are usually defined as the total derivative of the energy with respect to the ionic positions

$$\mathbf{F} = -\frac{d\,E}{d\mathbf{R}} \qquad (19)$$

In the PAW method (as in the US-PP method), complications arise from the fact that the augmentation spheres and compensation densities are allowed to move with the ions, which gives rise to additional terms (similar to Pulay forces) in comparison with standard plane-wave codes. These correction terms are described in detail by Kresse and Joubert [7], the generalisation to noncollinear magnetisation densities is straightforward.

Applications: Small metallic clusters

Small clusters of Fe_n ($n \leq 5$) have been studied extensively in the past and represent ideal systems for testing our implementation of noncollinear magnetism. As fcc Fe is known to have a spin-spiral ground-state, noncollinear magnetism is suggested to be important in Fe clusters, primarily as they have less symmetry constraints than bulk materials. The magnetic ground state of body-centred cubic chromium is a spin-density-wave state described as a long-period modulation (~ 20 interatomic distances) of a simple type-I antiferromagnetic structure [17], with a modest magnetic moment of $M_{Cr} \sim 0.6$ μ_B. However, there is evidence that in a case of

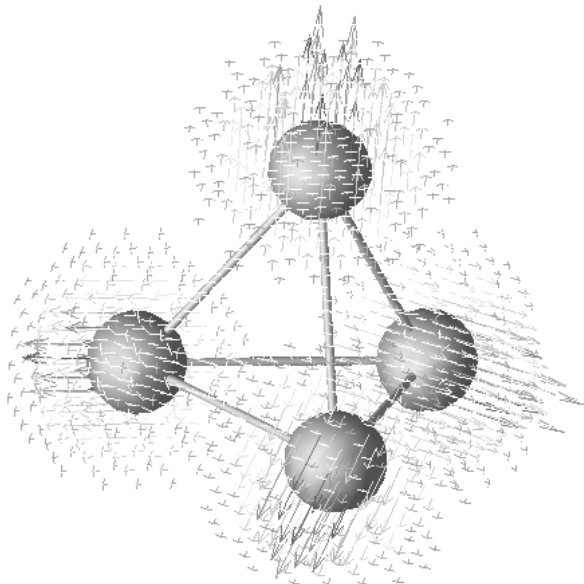Figure 2: A three dimensional view of the magnetisation density surrounding Cr_4 atoms. The iso-surface plots indicate that the magnetisation density is spherically symmetric at all large density values. Only in the 'Bloch wall' region does the direction of magnetisation change, the magnetic vectors rotate in the 'Bloch wall' but also tend to zero in this region.

reduced coordination (e.g. at a surface) the Cr moment is strongly enhanced - $M_{Cr} \sim 2.5\ \mu_B$ has been reported [18, 19] for a Cr(100) surface. With this in mind we have investigated the likely ground-state configurations of small Cr_n ($n \leq 5$) clusters. We expect large magnetic moments and strong antiferromagnetic nearest neighbour coupling. In the triangular like configurations this will inevitably lead to frustration and hence possibly to noncollinear states.

Tetrahedral Cr_4 is rather interesting in terms of noncollinear arrangements of the magnetic moments. We found three solutions, a metastable FM one with small bulk-like moments, a noncollinear metastable state, which is the 3D generalisation of the 120° arrangements found in frustrated antiferromagnetic 2D lattices with the magnetisation directions on the neighbouring atoms forming a tetrahedral angle of $\sim 109.5°$, and an AFM ground-state. In both the AFM and noncollinear states large magnetic moments are predicted. The AFM ground-state is $\sim$ 160 meV/atom (GGA) lower in energy than the noncollinear configuration. The structure is distorted unlike the FM and noncollinear cases with very large distances of 2.97 Å between ferromagnetically coupled atoms and slightly shorter bonds in AFM pairs. The noncollinear solution has a bond-length of 2.58 Å in GGA which is intermediate between the long bonds in the AFM and the short bonds in the FM configurations. In the noncollinear case the total atomic magnetic moment is $\sim 4.02\ \mu_B$/atom in the GGA and is symmetric on all sites. Fig. 2 shows a plot of the magnetisation density for this solution. The magnetisation density varies smoothly with position and is localised symmetrically around the atomic sites as depicted in Fig. 2.
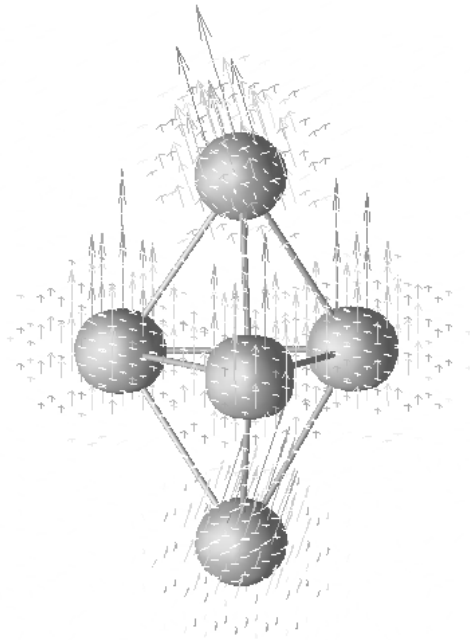

Figure 3: A three dimensional view of the magnetisation density surrounding Fe_5 atoms. The iso-surface plots indicate that the magnetisation density is spherically symmetric at all large density values on the apical atoms only, but is slightly 'squashed' at the central atomic sites. Only in the 'Bloch wall' region does the direction of magnetisation change, the magnetic vectors rotate in the 'Bloch wall' but also tend to zero in this region.

A case of particular interest in the work of Oda *et al.* [1] is the Fe_5 bipyramidal structure in which they found the roughly FM ground-state to contain tilted magnetic moments on the apical atoms of the bipyramid. Intuitively such solutions seem to be unphysical as they break the normal collinear symmetry and one would expect the total energy to be higher.

For the Fe$_5$ bipyramidal cluster our calculations have been able to stabilise a noncollinear solution some ~ 14 meV/atom below the collinear results. In the noncollinear ground-state as well as in the metastable collinear ferromagnetic state, the bond-lengths in the central triangle are slightly longer than between the central and the apical atoms. This somewhat squashed but otherwise undistorted structure agrees with the results of Oda *et al.* [1], but disagrees with the work of Castro and Salahub [20]. The tilt angle of the magnetic moment is $\sim 31.3°$ in GGA, to be compared to $\sim 29.7°$ in the LDA calculation of Oda *et al.* How such frustration might arise is not immediately clear. Certainly, the coupling between the apical atoms must play a crucial role in establishing the frustration. As the moments on the apical atoms tilt in opposite directions, it appears that the exchange interactions between the apical atoms is antiferromagnetic and hence acts against the ferromagnetic nearest neighbour coupling between apical and central atoms. Hence a rotation of the apical moments relative to those in the central triangle allows the magnetic energy to be optimised. A detailed analysis of the exchange coupling would be valuable to obtain better understanding of the conditions responsible for the frustration. Finally, Fig. 3 shows the magnetisation density surrounding the atomic sites. The figure illustrates, firstly, that the magnetisation density varies smoothly with position, secondly, that the spin-direction only changes at the 'Bloch wall' between atoms where the charge- and spin-densities are small and thirdly that the magnetisation density is roughly uniform in the magnetic region of the atoms. However, one can just see that for the central atoms the magnetisation density deviates from being spherically symmetric and exhibits a somewhat 'squashed' appearance.

Applications: Cr and Mn overlayers on the Cu(111) substrate
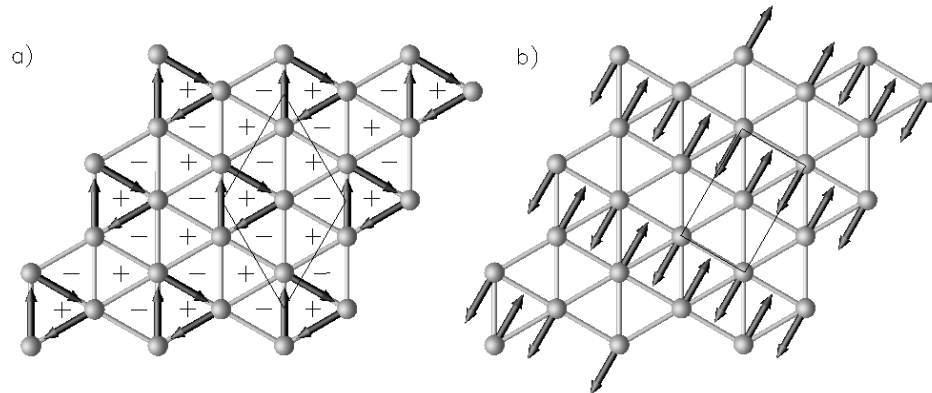

Figure 4: (a) Noncollinear magnetic structure of triangular layers corresponding to the frustrated XY-models with nearest-neighbour interactions. The relative directions of the magnetic moments (neglecting spin-orbit coupling) are indicated by the arrows. + and − signs indicate the helicities assigned to the elementary triangles (cf. text). The primitive ($\sqrt{3} \times \sqrt{3}$) unit cell is indicated by the thin lines. (b) Row-wise antiferromagnetic structure of triangular layers. Arrows indicate the relative directions of the magnetic moments, the thin lines show the c(2×2) unit cell.

One of the simplest examples of a frustrated two-dimensional spin system, where no perfectly collinear magnetic arrangement can be accommodated, is the antiferromagnetic planar (XY) model with nearest-neighbour interactions on a triangular lattice. Antiferromagnetic interactions

are a source of magnetic frustration on the triangular lattice. The ground states of such systems tend to consist of spins ordered on three interpenetrating sublattices with lattice vectors of length $\sqrt{3}a$ while spins on different sublattices are orientated $\pm120°$ to each other (see Fig. 4). Wannier [21] proved that by considering the ground state energy of any single elementary triangle and minimising the energy with respect to two of the spin angles one obtains ground states for the triangle in which the spins form $\pm120°$.

Freestanding triangular Cr and Mn monolayers

Fig. 5 summarises our results for the magnetic moments and total energies of the three possible magnetic configurations as a function of the nearest-neighbour bond-length. In both Cr and Mn monolayers, a ferromagnetic high-spin phase with a magnetic moment of nearly 4 μ_B is stable only at expanded interatomic distances. In Cr monolayers the magnetic moment breaks down rather suddenly at a bond-length of about 2.57 Å, the ferromagnetic minimum being about 280 meV higher in energy than the non-magnetic minimum. In Mn monolayers we find a transition from a ferromagnetic high-spin phase at bond-lengths larger than 2.47 Å to a ferromagnetic low-spin phase at closer interatomic distances. The low-spin phase (M $\leq$ 1.5 μ_B) looses its magnetic moment only at strongly reduced bond-lengths.

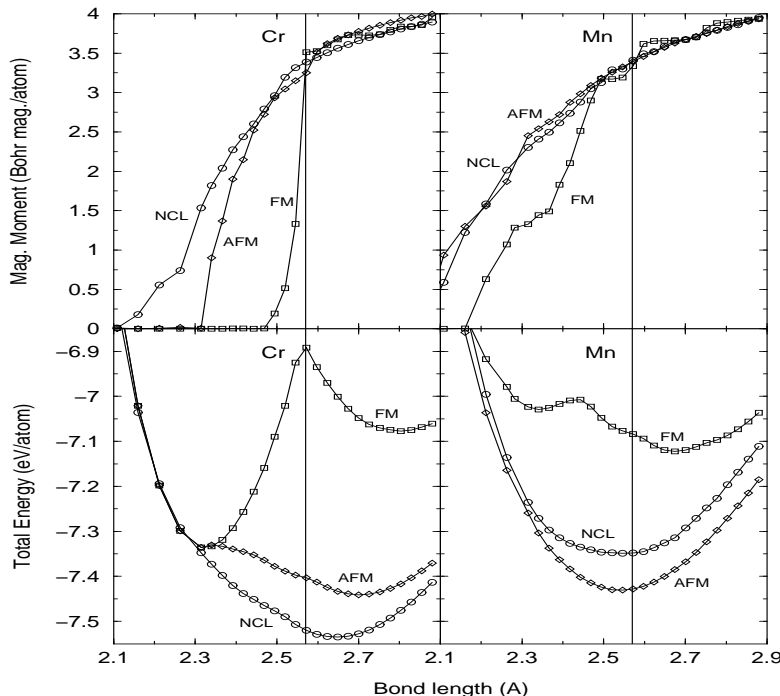Figure 5: Total energy and magnetic moments of the ferromagnetic $p(1 \times 1)$, the antiferromagnetic $c(2 \times 2)$, and the noncollinear ($\sqrt{3} \times \sqrt{3}$) phases of freestanding triangular Cr and Mn monolayers as a function of the nearest neighbour bond-length. The vertical lines mark the lateral interatomic distance of a Cu(111) substrate.

The row-wise antiferromagnetic $c(2 \times 2)$ Cr monolayer has an equilibrium bond-length of 2.70 Å at a magnetic moment of 3.75 μ_B. Under compression the magnetic moment is strongly reduced, it disappears at a bond-length of 2.31 Å corresponding roughly to the bond-length of the nonmagnetic phase. The noncollinear 120° phase represents the magnetic ground state, the equilibrium bond-length is about 2.65 Å, at these distances, the magnetic moment is slightly smaller

than in the antiferromagnetic phase. Under compression, the noncollinear magnetic moments are gradually reduced. They disappear at distances somewhat smaller than the equilibrium distances in the nonmagnetic phase.

In Mn monolayers the relative stability of the antiferromagnetic and noncollinear phase is reversed (see Fig 5), the equilibrium bond-lengths and magnetic moments being almost the same in both phases. Under compression the magnetic energy difference is quickly reduced, at bond-lengths smaller than about 2.35 Å, both phases are energetically almost degenerate. The antiferromagnetic ground-state in Mn is somewhat surprising, to investigate this point further we now consider triangular Cr and Mn overlayers on Cu(111).

Triangular Cr and Mn overlayers on Cu(111)

For overlayers adsorbed on Cu(111) substrates the same three magnetic configurations have been considered. For comparison, the vertical lines in Fig. 5 show the lateral lattice constant of the Cu(111) substrate. We find that triangular Mn-layers show an almost ideal epitaxial match to the substrate, whereas adsorbed Cr-layers undergo a small compressive strain. In both the antiferromagnetic and the noncollinear phases, the magnetic moments are reduced compared to the freestanding monolayer. The important point is that for Mn/Cu(111) the antiferromagnetic phase remains energetically favoured.
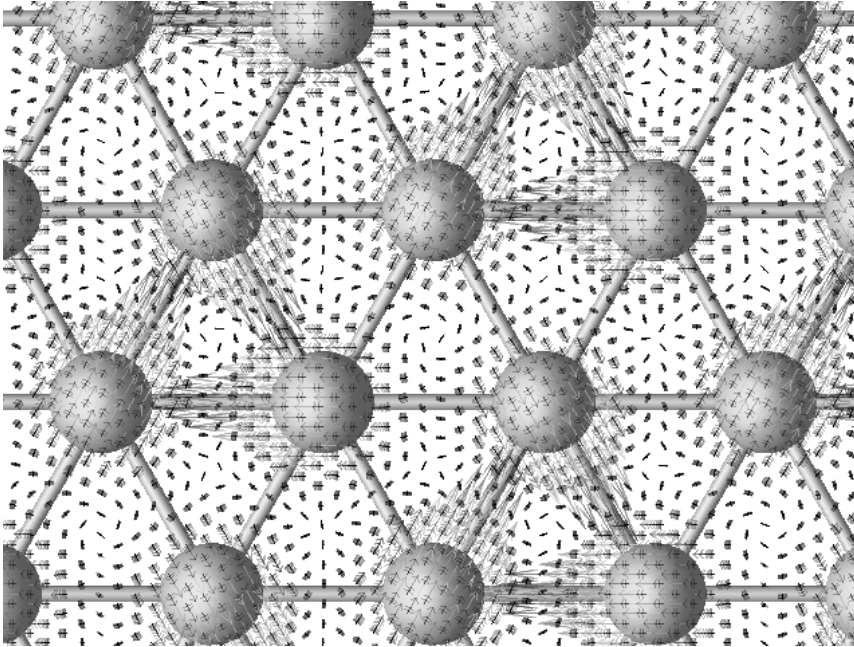

Figure 6: Vector field of the magnetisation density for the noncollinear phase of Cr on Cu(111). The relative direction of the magnetisation density (neglecting spin-orbit coupling) is indicated by the arrows, the length of each arrow is proportional to the absolute value of the local magnetisation density.

The different behaviour of triangular layers of Cr and Mn is clearly related to the rather long-range nature of the exchange interactions in the Mn layers, as already pointed out by Spišák and Hafner [22]. In the noncollinear phase, first and third neighbours carry magnetic moments with a relative 120° orientation, but second neighbour-moments are ferromagnetically aligned (see Fig. 4). In the row-wise antiferromagnetic structure out of six nearest and next-

nearest-neighbour atoms four are aligned antiferromagnetically and two ferromagnetically in each shell. All six sites in the third-neighbour shell show ferromagnetic alignment. If the exchange-interaction is antiferromagnetic for the first two shells and ferromagnetic for the third shell, the frustration may be weaker in the collinear phase.

Fig. 6 shows the magnetisation density calculated for the noncollinear phase of Cr on Cu(111). The local direction of the magnetic moment is indicated by the arrows, the length of the arrows being proportional to the absolute value of the magnetisation density. In addition, around each site iso-surfaces of the magnetisation densities are drawn. At a first look one tends to conclude that the magnetisation densities are fairly well localised and as the iso-surfaces are also almost spherical at reasonably large values, the conclusion that the AMA is a reasonable choice in this system seems to be appropriate. However, the regions around the atoms in which the direction of magnetisation is approximately constant are distinctly smaller than the muffin-tin spheres of the FLAPW method or the overlapping atomic spheres of the LMTO approach. Interesting new aspects of this study are seen precisely in the bonding and interstitial regions where the direction of the magnetisation changes.
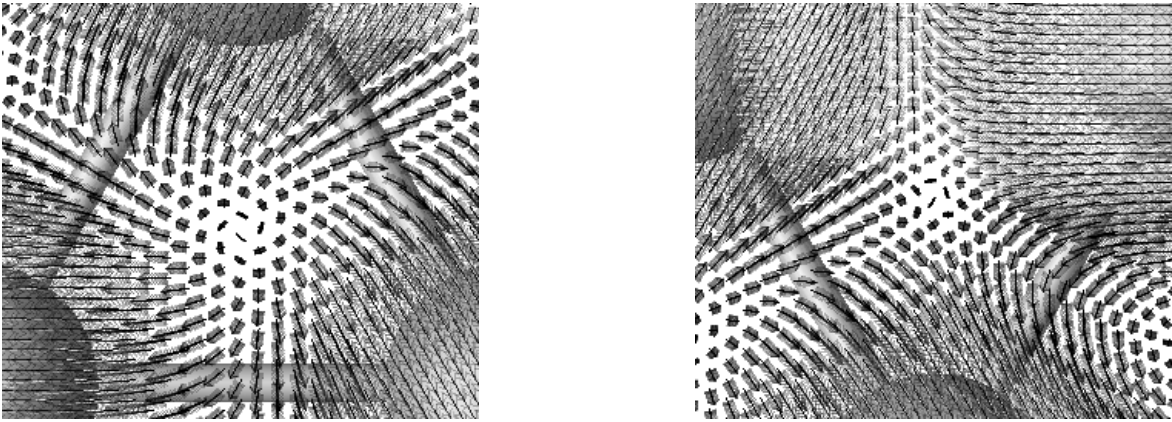

Figure 7: Enlarged view of an outward spiral-vortex and an anti-vortex. Cf. text.

In Figs. 7 and 8 we recognise characteristic patterns in the vector field of the magnetisation density: Inside the elementary triangles to which a positive helicity has been assigned, the vector field forms a vortex which may be a clockwise or a counterclockwise spiral or show a circular pattern, inside the triangles with negative helicity we find anti-vortex patterns related to each other by 120° rotations. Detailed views of the three types of vortices are show in Figs. 7 and 8. Spiral vortices are formed inside the triangles where the direction of the magnetisation is aligned (for the given alignment of the magnetisation directions with respect to the crystal lattice) along the bond directions, pointing either away from or into the triangle. In both cases the direction of magnetisation in the bond centres is perpendicular to the bonds, in the former case the vectors point out of the triangle and an outward spiral is formed, in the latter case the vectors point towards the centre of the triangle such that an inward spiral is formed. A circular vortex is formed within those triangles where the magnetisation at the lattice sites is perpendicular to one of the edges of the triangle. In the bond centres, the magnetisation is in this case aligned along the bond directions. An example for an anti-vortex structure realized in triangles with negative helicity is shown on the right side of Fig. 7. In this case the direction of magnetisation is perpendicular to two of the bonds (pointing either out of or into the triangle) and parallel

to the third bond. To the three different types of vortices correspond anti-vortex structures rotated by 120°. This picture also illustrates an important difference between the muffin-tin-like
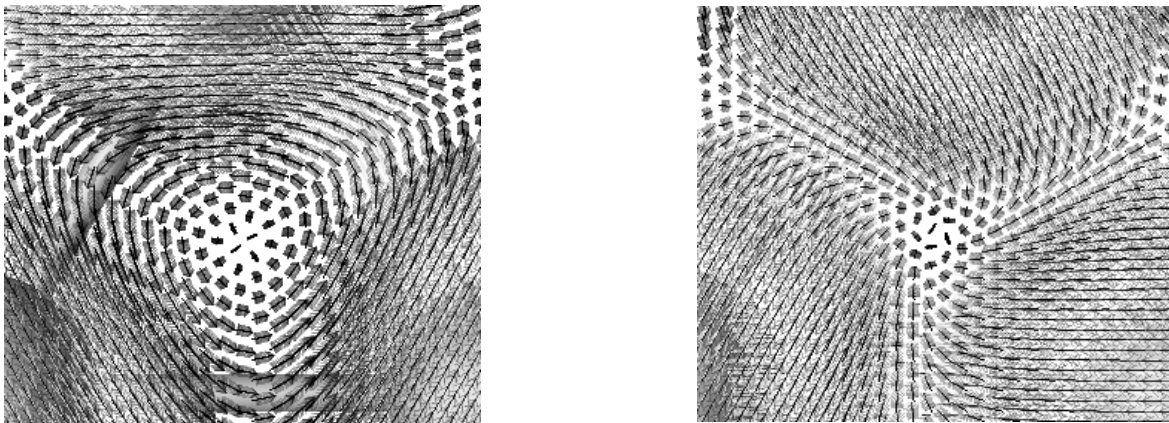

Figure 8: Enlarged view of a circular vortex and an inward spiral-vortex. Cf. text.

description of the magnetisation density within the FLAPW approach used by Asada *et al.* [4] and Kurz *et al.* [5] and the present PAW description. In the FLAPW-approach, the direction of magnetisation changes discontinuously at the muffin tin sphere boundaries. In the PAW description, the direction of magnetisation changes continuously and is (for the present choice of the global alignment) at these points either parallel or perpendicular to the bond, depending on its local environment. It is also interesting to point out that the bond-centres form a Kagomé lattice dual to the triangular lattice of the atoms. The six triangles surrounding a hexagon of the Kagomé lattice contain an alternating anti-vortex or vortex, the existence of three different types leading to further symmetry breaking analogous to the positive and negative helicities. This point certainly deserves further investigation.

Expected Impact

The approach described above has clearly been developed with the intention of studying problems in which magnetisation density is not well localised on atomic sites, in addition to more conventional cases. Examples of such weak localisation, for which the atomic moment approximation is more questionable, occur in materials such as disordered magnetic intermetallic compounds, amorphous alloys and structures with antiferromagnetically coupled atoms on sublattices necessarily leading to frustration (e.g. triangular layers and Kagomé lattices). As advancing computer technology allows us to explore more complex atomic structures such an approach will hopefully prove invaluable.

Acknowledgements

References

[1] T. Oda, A. Pasquarello, and R. Car, Phys. Rev. Lett. **80**, 3622 (1998).

[2] O. Ivanov and V. P. Antropov, J. Appl. Phys. **85**, 4821 (1999).

[3] L. Nordström and D. J. Singh, Phys. Rev. Lett. **76**, 4420 (1996).

[4] T. Asada, G. Bihlmayer, S. Handschuh, S. Heinze, Ph. Kurz, and Blügel, J. Phys.: Condens. Matter **11**, 9347 (1999).

[5] Ph. Kurz, G. Bihlmayer, F. Förster, S. Blügel, and L. Nordström, Ψ_k Newsletter **38**, 64 (2000).

[6] P. Blöchl, Phys. Rev. B **50**, 17953 (1994).

[7] G. Kresse and D. Joubert, Phys. Rev. B **59**, 1758 (1999).

[8] D. Vanderbilt, Phys. Rev. B **41**, 7892 (1990).

[9] G. Kresse and J. Hafner, J. Phys.:Condens. Matter **6**, 8245 (1994).

[10] http://www.cms.at/vasp/

[11] D. Hobbs, G. Kresse, and J. Hafner, Phys. Rev. B submitted (2000).

[12] D. Hobbs and J. Hafner, J. Phys.: Condens. Matter accepted June (2000).

[13] U. von Barth and L. Hedin, J. Phys. C: Solid State Phys. **5**, 1629 (1972).

[14] J. Kübler, K. H. Höck, and J. Sticht, J. Appl. Phys. **63**, 3482 (1988).

[15] J. Kübler, K. H. Höck, J. Sticht, and A. R. Williams, J. Phys. F: Met. Phys. **18**, 469 (1988).

[16] The magnetisation density is calculated from the spin-density defined here, by multiplying by the factor $\frac{e\hbar}{mc}$.

[17] H. Zabel, J.Phys. Condens. Matter **11**, 9303 (1999).

[18] L. E. Klebanoff, S. W. Robey, G. Liu, and D. A. Shirley, Phys. Rev. B **31**, 6379 (1985).

[19] C. L. Fu and A. J. Freeman, Phys. Rev. B **33**, 1755 (1986).

[20] M. Castro and D. R. Salahub, Phys. Rev. B **49**, 11842 (1994).

[21] G. H. Wannier, Phys. Rev. **79**, 357 (1950).

[22] D. Spišák and J. Hafner, Phys. Rev. B **61**, 12728 (2000).